Journal of Infrared, Millimeter, and Terahertz Waves (2023) 44:430–457
https://doi.org/10.1007/s10762-023-00916-3

Design and Characterization of Terahertz CORPS Beam Forming Networks

Carlos Biurrun-Quel[1] · Thomas Haddad[2] · Benedikt Sievert[3] · Robin Kress[4] · Nils Weimann[4] · Daniel Erni[3] · Andreas Rennings[3] · Andreas Stöhr[2] · Jorge Teniente[1] · Carlos del-Río[1]

Received: 6 December 2022 / Accepted: 20 March 2023 / Published online: 4 July 2023

Abstract

This work reviews the design and applicability of beam-forming networks based on Coherently Radiating Periodic Structures (CORPS-BFN) at Terahertz (THz) frequency bands. These versatile networks offer two operation modes: a continuous beam steering – feeding an antenna array with a linearly progressive phase distribution – using a reduced number of phase controls; or a multi-beam operation, generating independent, overlapped beams. These networks are built upon the concatenation of power combiners/dividers (PCDs) with isolated outputs. The isolation is provided by monolithically integrated resistors, implemented with Ti/TiO_2 thin films for the first time. In this work, a planar prototype of a 2×3 (inputs/outputs) microstrip CORPS-BFN for operation in the WR3.4/WM-864 band (220–330 GHz) on a thin 50 μm Indium Phosphide (InP) substrate is designed, fabricated, and characterized. The measured S-parameters show a reflection coefficient better than -15 dB and an insertion loss between 1.6 and 3.2 dB in the whole band. In addition, an isolation better than 20 dB between the input ports has been measured. An overall remarkable agreement is observed between the measurements and the simulations. Last, the applications, scalability and efficiency of this type of networks at the targeted band are discussed in detail.

✉ Carlos Biurrun-Quel
carlos.biurrun@unavarra.es

1 Antenna Group — Institute of Smart Cities, Department of Electrical, Electronic and Communication Engineering, Public University of Navarra, E-31006 Pamplona, Spain

2 Department of Optoelectronics, University Duisburg-Essen, D-47057 Duisburg, Germany

3 General and Theoreticel Electrical Engineering (ATE), University of Duisburg-Essen, and Center for Nanointegration Duisburg-Essen (CENIDE), D-47048 Duisburg, Germany

4 Department of Components for High-Frequency Electronics, University Duisburg-Essen, D-47057 Duisburg, Germany

Keywords Beam forming networks · CORPS · Indium phosphide · Monolithic integration · Terahertz · Thin-film

1 Introduction

A steady development and improvement of sources capable of generating Terahertz (THz) waves, namely, from 10^{11} to 10^{13} Hz, has taken place in the last decades, opening the doors to a plethora of stimulating applications such as spectroscopy [1], [2], imaging [3–5] or high capacity communications [6–8]. As a result, the so-called "Terahertz Gap" is shrinking due to the combined efforts of electronics and photonics scientists and engineers. However, despite presenting a promising future, THz sources still face a key challenge: efficiency in power generation [9]; and, whereas both electronic and photonic based THz sources [10, 11] present their own limitations and advantages, the overall conclusion is that the available THz power is limited. Furthermore, the spherical propagation of waves incurs in a path loss that is inversely proportional to the wavelength squared, which is especially challenging at THz frequencies. Consequently, the range of these systems is limited. Whereas some solutions employ bulky reflectors or lenses to increase gain (hence, increase range), another practical approach is to conform antenna arrays and perform beam forming techniques to focus the radiated power in the direction of interest. In addition, some THz applications, such as short-range mobile and machine-to-machine communications, require precise beam control techniques [12] for orienting the beam towards different directions. With this regard, one could differentiate between a multi-beam antenna system, where a single beam is selected out of a number of pre-defined beams (Beam Switching), and a steerable solution, in which a single beam is continuously redirected towards the direction of interest (Beam Steering). These two configurations are sketched in Fig. 1.

As for beam switching solutions, one traditional approach is to use multi-beam BFNs, such as Blass [13] or Butler [14] matrices, which control the propagation of the incoming signals at the input ports, tailoring the desired amplitude and phase distribution to the antenna elements. As a result, a number 'N' of different beams (being 'N' the number of input ports in the BFN), can be generated. These traditional solutions from the RF domain have scarcely been explored at the THz domain, with few examples found [15]. Other solutions to perform such multi-beam functionality is the use of lenses [16], which can be realized as a planar lens, (such as Rotman Lens [17] or Luneburg Lens [18]) or as a bulky, 3D lens, in which different feed positions with respect to the lens' focus generate different radiated beam directions [19]. In multi-beam systems, it is typically desired to have an angular resolution as fine as possible — namely, that the orthogonally generated beams are as narrow and as close in space as possible — so that two objects close to each other can be distinguished at far field. However, the solutions presented above are limited in resolution due to the physical size (aperture) of the radiating elements. This resolution issue can be overcome by using overlapped beams [20, 21].

On the other hand, phased arrays (PAs) - where a specific beam forming network (BFN) controls the input signal's phase and magnitude for each antenna element - stand out as one of the most versatile solutions in terms of performance. They are capable

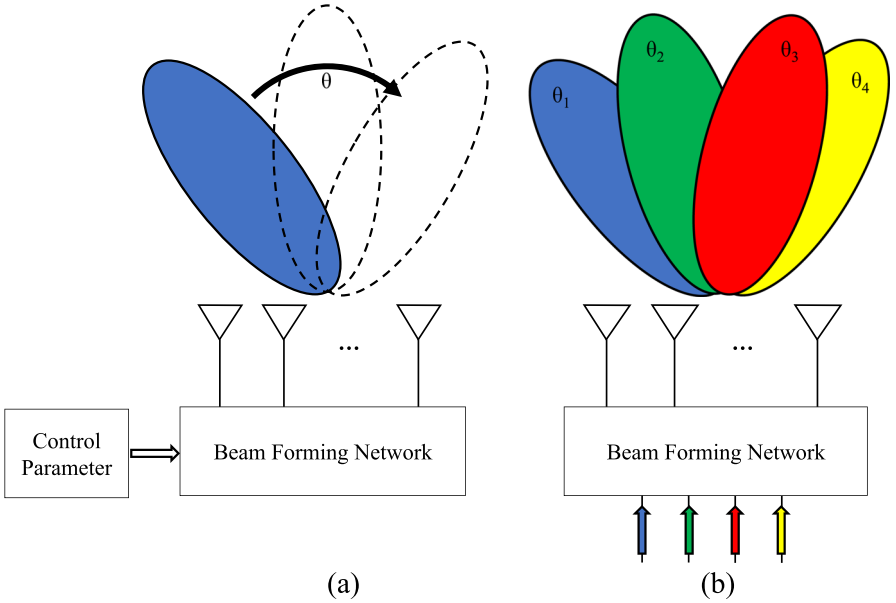

Fig. 1 Illustration of the difference between (a) Beam Steering, where a control parameter (such as a phase difference) defines the beam direction; and (b) Beam switching, where the BFN and antenna array is shared by different inputs, and each input generates a different radiation pattern

of providing a dynamic and continuous beam steering across different angles when carefully designed, which is realizable in either 1D or 2D. Many implementations, however, require individual amplitude and phase controls for each antenna element, which might pose scalability issues for larger arrays in terms of cost, space and complexity. In fact, one main limitation in the broad implementation of phased arrays in THz domain is the lack of efficient phase shifters at these frequencies. Whereas some electronically fed THz phased array solutions have been demonstrated recently [22, 23] and phase-shifters based on liquid crystals [24–26] or coupled PLLs [27] show promising results, other solutions for generating the desired phase distributions based on frequency conversion have been proposed. For instance, down-conversion from optical sources by difference-frequency generation or "photomixing" [28] allows controlling the phase of the optical beats by using optical delay lines (ODLs) [29, 30]. However, the need for a dedicated ODL for each element in the array might as well compromise its scalability.

In this context, BFNs based on Coherently Radiating Periodic Structures (CORPS-BFN) — consisting of simple passive power combiners/dividers — seem an interesting alternative, since they are able to offer both, beam steering and switching operation [31, 32]. For instance, this type of networks has recently been proposed for feeding a reflector-based Synthetic Aperture Radar (SAR) at L-Band (1.25 GHz) [21]. In such application, the resolution of the system is enhanced thanks to the capability of CORPS-BFN to generate overlapped beams. In addition, our recent work [33] demonstrated the integration of a 2×3 CORPS-BFN together with an array of Leaky

Wave Antennas, performing a controlled 2D beam steering in the WR3.4/WM-864 band (220–330 GHz) with a minimum number of controls (namely two: the operational frequency controlling the beam steering along the H-plane and an ODL controlling the steering along the E-plane).

That work constituted the first implementation of a CORPS-BFN above 10 GHz. However, little attention was paid to the network itself, how to design it, or its potential applications. Therefore, the aim of this paper is to shed light onto the principle of operation of these type of networks and discuss their potential uses at THz frequencies. For this purpose, useful design and fabrication guidelines are provided, including the development of monolithically integrated resistors. In addition, a prototype of a 2×3 CORPS-BFN is fully characterized. The remainder of the paper is structured as follows: Sect. 2 reviews operation principle and state of the art of CORPS-BFN. The methodology followed to design and fabricate a prototype consisting of a single-layer THz CORPS-BFN composed by Wilkinson Power Combiner/Dividers (WPCDs) is detailed in Sect. 3. The prototype, with two inputs and three outputs, operates at around 300 GHz and was designed and manufactured on microstrip technology with standard photolithography on a 50 μm thick Indium Phosphide (InP) substrate. On-wafer characterization of the network and the WPCDs is presented in Sect. 4. The scalability of the network and applicability in the THz domain is then discussed in Sect. 5. Last, some outlook into future research is provided.

2 CORPS-BFN

Coherently Radiating Periodic Structures (CORPS) were proposed at the beginning of the current century to enhance the radiation properties of phased arrays [34]. This concept was soon extrapolated to the field of BFN [35], namely CORPS-BFN. These networks consist of 'L' layers composed of Split (S) and Re-combination (R) nodes, which essentially are standard power combiner/dividers (PCDs) with isolated outputs, such as Wilkinson [36] or Gysel [37] power dividers/combiners. A general representation of a CORPS-BFN and its modes of operation is provided in Fig. 2. Here, it can be seen that each layer starts at the inputs of the S-nodes and ends at the outputs of the R-nodes, in a way that these outputs are connected to the inputs of the next layer (or to the antenna elements, in case of the last layer). Since every S and R-node are implemented by the same device, every path across each layer is electrically equivalent and the signal is split and recombined in-phase (coherently).

Moreover, the isolation between the outputs of these nodes allows controlling the spread of the power within each layer and therefore, within the whole multilayer structure.

As a result, a standard L-layer CORPS-BFN can feed an N-element linear array with just M input ports, where N=M+L. Individually, every single input port reaches up to L+1 radiating elements, which enables the definition of different overlapped sub-arrays thanks to the antenna sharing between the inputs. Additionally, due to the isolation provided by the PCDs, the beams generated by each sub-array are orthogonal to each other, what makes them very interesting candidates for multi-beam operation, as already demonstrated for satellite systems [21, 32]. In addition, the network can

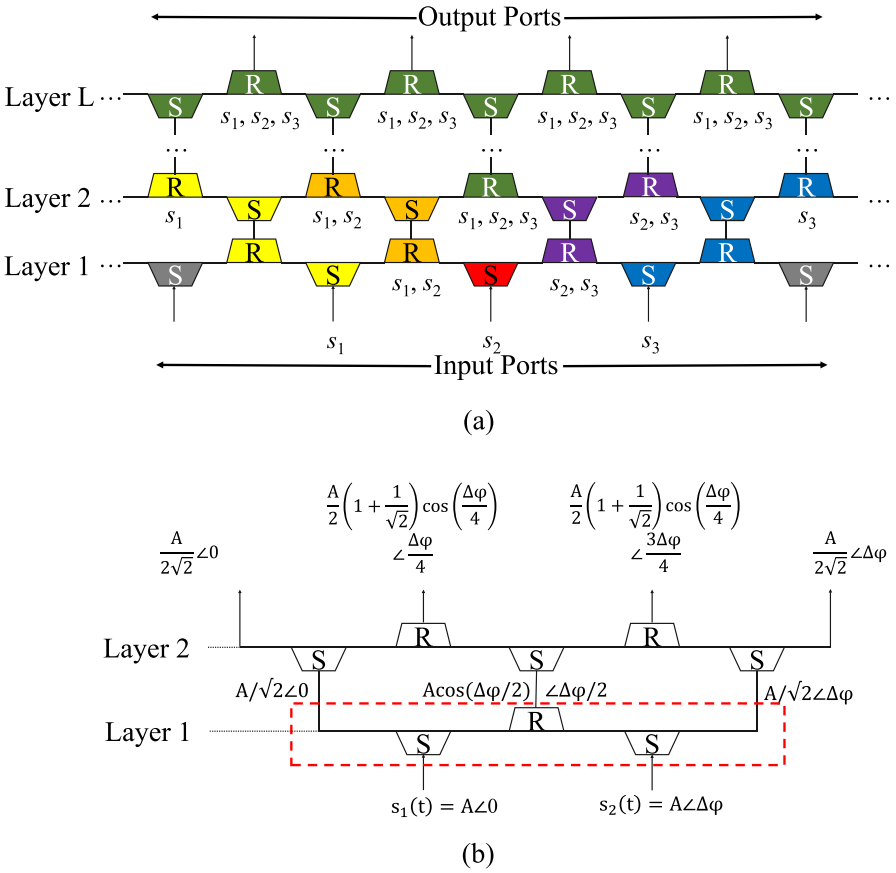

Fig. 2 CORPS-BFN modes of operation (a) Beam Switching. Different colours illustrate the propagation of different signals and element sharing across the network (b) Beam Steering with relative amplitude and phase at each point (Red box: sub-network presented in this work)

also be operated to perform a continuous beam steering by simultaneously feeding two contiguous input ports with a controlled relative phase shift, as demonstrated recently in [33] and depicted in Fig. 2 (b). In this case, an averaging process takes place in the recombination nodes, obtaining an averaged relative phase at their their outputs at the expense of a penalty in the amplitude of the signal (cosine term) proportional to a half of the relative phase difference between the the inputs. As a result, for a phase difference $\Delta\varphi$ between the inputs, a linearly progressive phase distribution with step $\Delta\varphi/2$ would be realizable with a single-layer CORPS-BFN. As it can be seen in Fig. 2(b), increasing the number of layers would incur in a non linear progression at the outputs. Whereas this issue may impose a limitation for a linear array where every antenna element is separated at a distance d, such limitation can be avoided by tailoring the distance between antenna elements. For instance, the second and third antennas in Layer 2 should be separated at twice the distance d to achieve a fully

constructive interference in the far-field, as described by the computation of the array factor in a linear array [38] as described by Eq. 1:

$$AF(\theta, \phi) = \sum_{\mathrm{i}}^{\mathrm{N}} A_{\mathrm{i}} \mathrm{e}^{j\phi_{\mathrm{i}} \mathrm{k}_0 d(\mathrm{i}-1)\cos\theta \sin\phi}. \quad (1)$$

However, this would incur in a reduced aperture efficiency, as the resulting array would be equivalent in size to a 5-element array with the central element missing ($A_3 = 0$). In addition, the inclusion of more layers will incur in higher losses, since more R-nodes performing averages between delayed signals will be involved. As a result, the most efficient CORPS-BFN topology for performing beam steering is a 2×3 block. This is not necessarily the case for its multi-beam operation. In this case, the most efficient topology will be that providing the highest antenna-gain/insertion-loss ratio, as analyzed in [39].

At this point, the versatility and capabilities of this type of networks have been presented. On the one hand, we believe that the multi-beam features of the CORPS-BFN could be of great use for Terahertz imaging systems with increased angular resolution, thanks to the capability of overlapping beams and overcoming the limitation fixed by the aperture size of the radiating elements. On the other hand, a cost-effective beam steering solution could be implemented by using a single-layered 2×3 (input/output) CORPS-BFN. In order to assess the actual performance of this type of networks in the THz regime, a 2×3 CORPS-BFN prototype was designed, fabricated and characterized for its operation within the WR3.4 band (220–330 GHz) (Eq. 1).

3 Design of a CORPS-BFN

In this work, a CORPS-BFN was designed on a 50μm thick grounded InP substrate (ϵ_r = 12.4, tan δ = 0.002 [40]). The targeted frequency was the band comprehending from 270 to 320 GHz, although the network exhibited a broadband behaviour all across the WR3.4 band. The thin thickness of the substrate allows minimizing the number of substrate modes present, as explained in [41], pushing the cut-off frequency of TE_1 and TM_1 modes above 400 GHz (inevitably propagating the TM_0). This substrate material was chosen to target a realistic scenario where a THz source would be integrated, such as III-V Unitraveling Carrier photodiodes (UTC-PDs) [42], Resonant Tunneling Diodes (RTDs) [43], or Heterojunction Bipolar Transistors (HBT) [44] The constitutive element of the network — namely, the Wilkinson power combiner/divider (WPCD) — was designed as a first step. Despite having higher losses than coplanar waveguide technology (CPW), microstrip technology was chosen to implement this THz prototype for two main reasons. First, this technology allows direct integration with a plethora of planar antennas, and, secondly, it facilitates the implementation of the resistor in the WPCD. With this implementation, no wire-bonds, air bridges, nor complicated configurations are needed (in contrast to more challenging - though remarkable - CPW implementations of WPCD such as the one found in [22]). In our work, the dimensions of the WPCD were significantly small due to the high frequency of operation and permittivity of the substrate. Consequently, the integrated resistors

were implemented by means of thin-film technology. The characterization and design procedure of such integrated resistors is tackled in Sect. 3.6. The chosen material to implement these resistors was Titanium, which was reported to present a small Temperature Coefficient Resistance (TCR) and allows implementing a relatively wide range of resistances [45]. In addition, this material oxidizes at ambient conditions, creating a thin TiO_2 passivation layer.

In order to design a CORPS-BFN, the following methodology is proposed: First, the WPCD (S/R-node) must be chosen and designed carefully. For this purpose, the properties of each line section must be tailored to obtain a broadband device. As such, a study of the electrical properties of microstrip lines on Indium Phosphide (InP) was carried out. Next, once the WPCD has been defined and developed, the whole BFN is built with the proper arrangement of S/R-nodes and delay lines. Furthermore, a constraint in the distance between the outputs of the network (distance between antennas) was considered, since in a practical application the antennas must be located at a specific distance (typically $\lambda/2$ to avoid grating lobes when steering the beam). One last concern to bear in mind is that special care must be taken during the designing stage, so that every path is electrically equivalent after dividing the input signal, which must reach the corresponding outputs with the same relative phase.

3.1 Determination of Electrical Properties

Whereas approximated expressions for both the effective permittivity and impedance of microstrip lines are given in Chapter 3 in [46], these expressions fail to provide frequency-dependent values because they assume the quasi-TEM approximation. In contrast to these expressions, finite element simulations carried out in commercial software, such as ANSYS HFSS [47], offer accurate and frequency-dependent information (at the expense of computation time) about the propagation constant, wave impedance, and effective dielectric constant of every mode propagating in a transmission line by computing 2D Eigenmode solutions on a planar, well-meshed wave port. A short section of microstrip enclosed between two wave ports was simulated in HFSS, sweeping its linewidth between 5 and 75 μm to obtain the desired

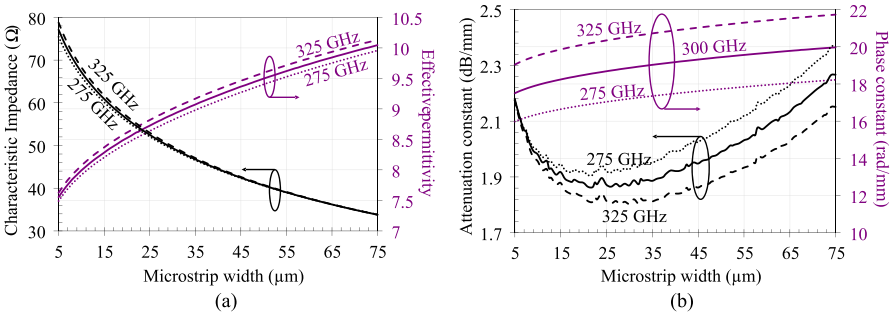

Fig. 3 Electrical properties of the lines with respect to their width (a) Characteristic impedance and effective permittivity. (b) Propagation constant (attenuation and phase). Results at 275 (dotted), 300 (solid) and 325 GHz (dashed)

characteristics for its fundamental mode calculated at three frequency points, between 275 to 325 GHz. The fine mesh employed provided a precision (difference between the values obtained for each wave port) in the worst case of ±0.05 Ω in computing the characteristic impedance and ±0.01 in the computation of the effective permittivity. Figure 3 provides a comprehensive summary of the results obtained in the simulation. The left and right ordinate axis in (a) represent the characteristic impedance and effective permittivity of the line for each simulated linewidth at 300 GHz. It is worth noting that the characteristic impedance of the narrowest lines presented a strong frequency dependence, whereas this dependence becomes less significant for wider lines. As for the effective permittivity, it was observed that it increased with increasing linewidth (as expected from the quasi-TEM formulas), with as small variation within the frequency band. Information regarding the propagation constant of the line ($\gamma = \alpha + j\beta$) was also obtained and is summarized in Fig. 3 (b). The phase constant computed by HFSS corresponds to the expected theoretical value ($\beta = 2\pi/\lambda_g$, where $\lambda_g = \lambda/\sqrt{\epsilon_{eff}}$) and due to its dependence on the effective permittivity, increases for wider lines. The simulation provided a worst-case accuracy of ±0.001 Np/mm (less than 0.01 dB/mm) concerning the attenuation constant, which was observed to represent a concave function, with its minimum values found at linewidths between 20 and 30 µm.

3.2 Design of the Wilkinson Power Combiner/Divider

The designed WPCD is illustrated in Fig. 4 (a) with its main dimensions of interest, whereas (b) provides its circuital representation. A summarized view of every line section, and their dimensions and electrical properties is provided in Table 1. It is worth noting that the outputs of the WPCD were separated to a distance d_{ant}, namely the antenna separation in a real scenario, which in this case corresponds to 480 µm (slightly lower than $\lambda/2$ @ 300 GHz). On the one hand, a more compact power divider would be implemented without this specific requirement, hence reducing its insertion loss. On the other hand, this requirement imposed the need for additional line sections, which was harnessed by selectively tuning the impedance and the length of each section to optimize the overall performance (in terms of impedance matching

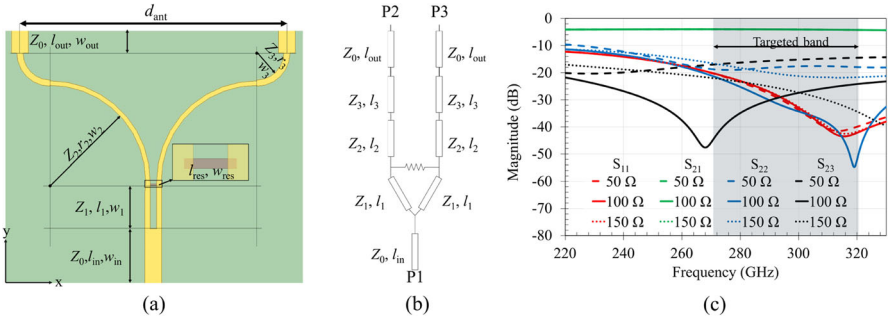

Fig. 4 Wilkinson Power Combiner Divider (WPCD). a) Layout of the device. b) Equivalent circuit. (c) Simulated S-Parameters of the WPCD. Deviation of ±50 Ω in resistance from an ideal value of 100 Ω is depicted with discontinuous lines. S-matrix is reciprocal

Table 1 Main dimensions and electrical properties of each WPCD line section at 300 GHz

Dimension	In.Line $Z_0, l_{\text{in}}, w_{\text{in}}$	Line 1 Z_1, l_1, w_1	Line 2 Z_2, l_2, w_2	Line 3 Z_3, l_3, w_3	Out. Line $Z_0, l_{\text{out}}, w_{\text{out}}$
Width, w (μm)	30	9	8	11	30
Eff. permit, ϵ_{eff}	8.99	8.07	8.00	8.20	8.99
Phy. Length, l (μm)	100	68	270	85	42
El. Length, $\theta(^\circ)$	108	69	276	88	45
Ch. Imped, Z_0	50.7	70.6	72.4	65.7	50.7

and port isolation). Every port was considered to have a standardized characteristic impedance of Z_0=50 Ω, although the resolution in our photolithography process (1 μm) imposed as well a limitation in the resolution of each line characteristic impedance. Following the canonical design procedure of a WPCD, the resistor was designed to have an approximate resistance of 100 Ω, consisting of 15 μm long (l_{res}), 4 μm wide (w_{res}) films with an electrical conductivity of 154 kS/m (see Sect. 3.6). It was also assumed that the integrated resistor would not provide just the desired resistance but also a parasitic inductance, affecting the overall impedance match. This parasitic reactance is intrinsically included in the analysis using full-wave electromagnetic (EM) simulation. A nanometre-scale mesh was set in this area to ensure an accurate EM simulation of the resistor. Microstrip lines with a thickness of 1.2 μm of copper and a gold coating of 75 nm, and an infinite golden ground plane were considered.

The device was simulated in the WR3.4 frequency band (220 to 330 GHz) though its performance was optimized from 270 to 320 GHz. Figure 4(c) presents the main scattering parameters obtained by full-wave simulation with HFSS, where $S_{21} = S_{31}$ and $S_{22} = S_{33}$ due to the device's symmetry. Three monomode microstrip wave ports were included, where P1 corresponds to the input port when the device operates as a power divider, and P2 and P3 are the respective outputs. It is observed that, for the nominal case (100 Ω resistors), the ports are matched with return losses (RL) higher than 10 dB for the whole WR3.4 band and over 20 dB in the band of interest. In addition, it is checked that the isolation of the output ports is above 20 dB for the whole WR3.4 band. Lastly, an insertion loss (IL) between 0.85 dB and 1 dB was obtained across the whole WR3.4 band. As a quick consistency validation, the total line length between ports 1 and 2 in the designed WPCD is 565μm, whereas Fig. 3 shows attenuation values around 1.9 dB/mm. The simulated IL is therefore consistent for different simulation set-ups. Furthermore, the influence of the resistor was studied by modifying the conductivity of the custom material, motivated by the uncertainty observed in the sheet resistance of the thin film characterization process – a matter which will be addressed later in Sect. 3.6. Overall, being the isolation between the output ports the most affected one. Figure 4(c) provides the maximum variation of the S-Parameters for a deviation of ±50 Ω in the resistance of the integrated resistor (dotted and dashed lines).

It can be checked that the lower resistance is the one which deteriorates the performance the most, shifting the minima of the port isolation to lower frequencies.

The reflection coefficient of the input port remained unaffected, whereas the reflection coefficient of the output ports varied slightly but stayed under -15dB in the band of interest. All these findings agree with the theoretical operation of the WPCD and previous circuital simulations in Keysight's ADS [48]. Hence, it is concluded that the resistor plays a major role in isolating the outputs and matching their port impedance but does not affect the input port matching nor the insertion loss.

3.3 Design of a 2 × 3 CORPS-BFN

Once the WPCD has been designed, building the CORPS-BFN results in a straightforward, scalable task. Recalling the rectangular section highlighted in Fig. 2(b), one can check that the prototype BFN (Fig. 5 (a)) is a combination of three WPCDs and additional line sections to match the phases of the outgoing signals (i.e., that the phase delay incurred by the network on the incoming signal at IN1 is the same after traveling to OUT1 and OUT2). Under the assumption of a lossless line scenario and considering ports 1–2 as inputs and 3–5 as the outputs, the ideal S-matrix of the network is:

$$S = \begin{pmatrix} 0 & 0 & \sqrt{1/2} & 1/2 & 0 \\ 0 & 0 & 0 & 1/2 & \sqrt{1/2} \\ \sqrt{1/2} & 0 & 0 & 0 & 0 \\ 1/2 & 1/2 & 0 & 0 & 0 \\ 0 & \sqrt{1/2} & 0 & 0 & 0 \end{pmatrix} \cdot e^{j\phi} \tag{2}$$

Here, the phase term implies that every path is electrically equivalent. Whereas the matrix corresponds to a lossy network, it can be checked that a joint operation of both inputs with the same incoming amplitude and phase results in the full recovery of the input power, distributed among the three outputs. Hence, the use this CORPS-BFN in beam switching applications, where every single port is operated individually, will be generally less efficient in terms of power than in a beam steering application. The most demanding issue encountered in this design stage was fitting the delay lines

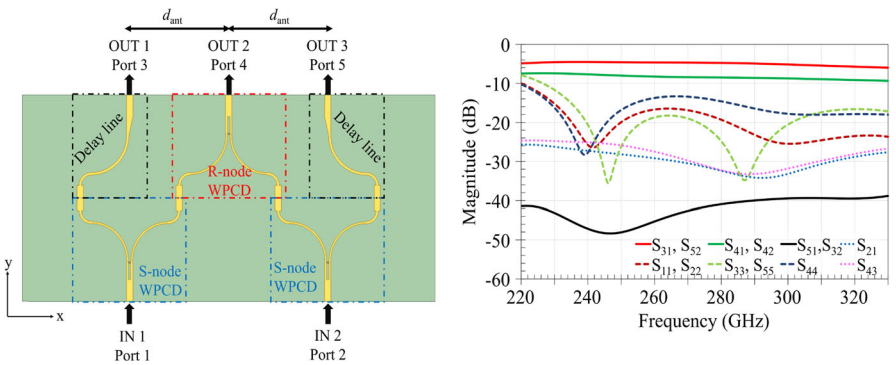

Fig. 5 Designed 2 × 3 CORPS-BFN based on WPCDs for a fixed distance between outputs. (a) Layout. (b) S-Parameters

to achieve broadband coherency for every non-isolated path in the network. This was limited by the predefined fixed distance between the output ports (d_{ant}), which resulted challenging due to the significant variation of the effective permittivity of the line for different linewidths. Furthermore, through simulation, it was observed that very narrow radii at the microstrip bends introduced different phase shifts and strong attenuations for each frequency. For these reasons, it was decided that the most straightforward way to achieve broadband phase matching was to reproduce the same curvature as the WPCD branches. Final impedance matching was solved by introducing a tapered line section with initial and final widths of 11μm and 30 μm, respectively.

The relevant S-Parameters of the network, simulated in HFSS, are displayed in Fig. 5(b). Every port is matched in the whole WR3.4 band with return losses above the 10 dB level and above 15 dB in the band of interest. In addition, the isolation between input ports (IN1 and IN2), output ports (OUT1, OUT2, OUT3), and among each input concerning its corresponding isolated output (S_{51}=S_{32}) remain above 20 dB for the whole WR3.4 band and above 30 dB for most part of the band of interest. The IL (with respect to the ideal matrix in Eq. 2) lays around 2 dB, which is consistent with previous results, since the network is essentially composed of two layers of WPCDs (with the delay lines having an equivalent electrical length), and each WPCD was inferring a 1 dB loss over the nominal -3dB of a power divider. As in the WPCD design stage, the influence of the resistors was assessed. This was made by performing a parametric sweep of their resistance. Overall, it was checked that the response was shifted to lower frequencies for increasing resistance. Nevertheless, it was observed that the significance of these variations was low, and that the essential features such as isolation between inputs/outputs, IL and RL remained close to the original reference levels.

On the other hand, the most relevant variation was not in magnitude, but in terms of phase. As previously explained in this section and discussed in [33], this coherent BFN must have electrically equivalent paths from one input to its corresponding outputs. Figure 6 plots the difference in terms of phase for the transmission parameters between

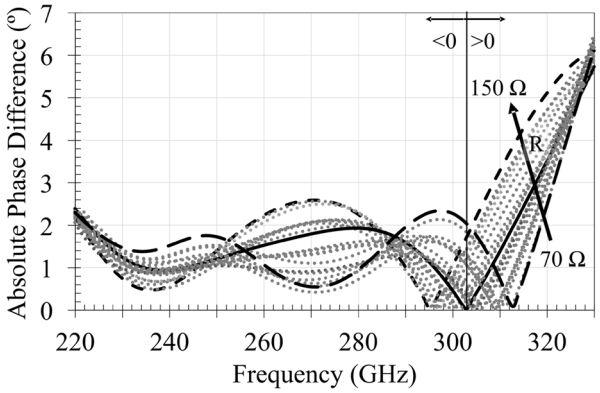

Fig. 6 Difference in phase introduced by the network for the signals travelling from Port 1 to Ports 3 and 4 (solid line) for 100 Ω resistors. Influence of resistance variation is also depicted (dotted and dashed lines)

Port 1 to Ports 3 and 4. The solid black line represents the original resistor value (100 Ω). The dashed lines represent the maximum variation observed in simulation for values of 70 and 150 Ω, whereas the dotted lines represent intermediate cases. It is worth noting that this figure represents an absolute value of the phase difference and that the transition from a negative to a positive phase difference is highlighted with a vertical line for the case of 100 Ω. This is attributed to the different electrical behavior of the tapered sections at the lateral output ports with respect to the tapered sections located at the central output together with the integrated resistor. The influence of this resistor is clearly observable by varying its resistance, concluding that it is responsible for this phase difference.

3.4 Design of CPW-to-Microstrip Transition

On-wafer characterization of planar mmWave and THz devices typically requires using waveguide extenders and GSG probes (ground-signal-ground), enabling the excitation of a coplanar mode. However, the WPCD and CORPS-BFN presented in this work were implemented in microstrip technology. Consequently, a transition was required. A compact Grounded Coplanar Waveguide (GCPW) to microstrip transition (Fig. 7(a) was targeted to reduce ohmic and dielectric losses, whose main dimensions are summarized in Table 2. The transition consists of three differentiated sections. The first corresponds to a 50 Ω grounded coplanar waveguide (GCPW). The minimum ground extension was set to ensure good contact of the probe tip (the pitch of the GSG probe was considered 100 µm). The second section serves two purposes: *First*, it broadens the slots of the CPW, while it shrinks the center conductor. As a result, the impedance of the coplanar mode increases (quasi-TEM expressions for this impedance are given in [49]), forcing the EM waves to couple in the microstrip mode. *Secondly*, this narrow strip constitutes a high impedance section as well, which serves as a good transition towards the microstrip mode for that part of the energy kept in the high-impedance CPW mode. The third line section consists of a 50 Ω microstrip line, which would be connected to the device to be measured.

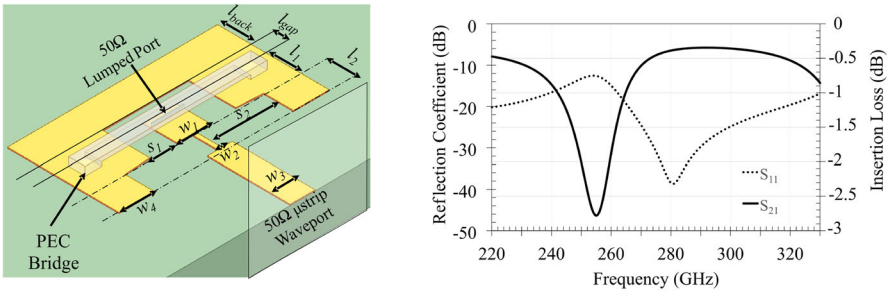

Fig. 7 GCPW to microstrip transition. a) 3D perspective with its main dimensions. The substrate is grounded at its backside. (b) Simulated S-Parameters

Table 2 Main dimensions of the GCPW to microstrip transition

Parameter	Value (μm)	Parameter	Value (μm)
w_1	40	s_1	32
l_1	40	w_2	5
s_2	81	l_2	33
w_3	30	w_4	43
l_{gap}	17	l_{back}	40

The (lumped) input port consists of a 5-μm-high, 32-μm-wide lumped port (as wide as the central conductor). A PEC bridge was included in the simulation to connect both lateral grounds to the lumped port, emulating the GSG probe. The simulated insertion loss and reflection coefficient of the transition are shown in Fig. 7(b). It can be seen that a reasonably low insertion loss is achieved (lower than 1 dB) while the return loss remains above 15 dB. A small resonance area is observed at around 254 GHz, where half of the power is lost due to radiation of the CPW outer pad. Nevertheless, the transition's performance is sufficiently stable from 263 to 330 GHz, comprehending our band of interest. The transition was included at every microstrip port in the WPCD and CORPS-BFN. In this regard, it is worth noting that the transition works without an existing electrical connection of the GND CPW pad with the bottom ground. Nevertheless, when performing the measurements with the GSG probes, a common DC GND reference (VNA) is provided to both CPW ports being measured. Last, since the transitions would obscure the S-parameter measurements, it became necessary to include a custom TRL (Thru-Reflect-Line) calibration kit [50] to de-embed its effect from the raw measured data. Such kit was also fabricated on-wafer.

3.5 Fabrication

The thin (50 μm) InP substrate was prepared following the process presented in [51]. Essentially, a thick InP wafer is bonded to a transfer substrate (i.e., Silicon) via thermally enhanced compression bonding with temperatures up to 250°C, carried out after deposition of a gold layer on the faces to be bonded. Once the wafers are bonded, the InP can be thinned down to the desired thickness with minimum risks. A chemical–mechanical polishing process follows this thinning process to ensure a flat, smooth surface. It is worth highlighting that without the transfer wafer, the crystalline structure of InP could be compromised during the thinning process, leading to the likely rupture of the wafer. Moreover, the transfer substrate facilitates the overall handling of the chip. The fabrication of the presented network was carried out through a multi-step standard photolithography process. It consisted of a two-step metallization and lift-off process, one for the thin-film resistors and a second one for the microstrip/CPW structures, both performed with a negative photoresist (AZ nLOF 2035). To produce the resistors of the WPCD circuits, 200 nm-thin films of Ti were deposited by controlled e-beam evaporation (Nexdep - Angstrom Engineering). The final Ti sheets were obtained by

lift-off of the exposed photoresist. It was observed that the mere lift-off process, which employs an aqueous-based etchant (*TechniStrip* NI555), produced a change in color of the films, which was attributed to an oxidation process. SEM pictures determined that the thickness of the films was 220 nm, denoting a lack of precision in the Ti deposition. As for the metallization of the circuit, an initial layer of 1.2 µm Cu coated by a layer of approximately 75 nm Au (to protect the copper from oxidation) were also deposited by e-beam evaporation. An average conductor thickness of 1,274 nm was measured, with a root-mean-squared (RMS) around 11 nm.

Last, it must be noted that the scattering parameters of a microwave network are defined between two ports, where every other port must be loaded with a matched impedance Z_0. The components to be fabricated, however, consisted of 3-port (WPCD) and 5-port (CORPS-BFN) networks. Hence, several copies of each (two of WPCD and six of CORPS-BFN) were needed to fully characterize the multiport, integrating the load resistors at different ports on each copy. Given that every copy was fabricated within the exact fabrication round, it was assumed that they were affected by the same tolerances, and the single measurements could be combined to characterize the whole component, taking into account some errors due to different positioning of the probes on each measurement should be expected. The required matched loads at the unconnected ports ($Z_0 = 50\ \Omega$) were implemented similarly to as the lumped resistors of the WPCD, with a film length of 23 µm and a width of 13 µm. Hence, some deviation regarding the desired 50Ω was expected due to the resistivity uncertainty. These loads were placed at the gap between the center conductor and the ground of the CPW pads. Full wave simulations were performed to ensure that the load impedance offered by the thin films together with the transition were approximately 50 Ω. However, whereas this was true for the real part of the load impedance, a reactance was introduced by the coplanar pad, increasing from -25Ω at 260 GHz to 15 Ω at 330 GHz. Nevertheless, the S_{11} simulated at the load resistors was better than -15 dB in the band of interest. Some of the fabricated structures are shown in Fig. 8, where the two different thin-film resistors are highlighted.

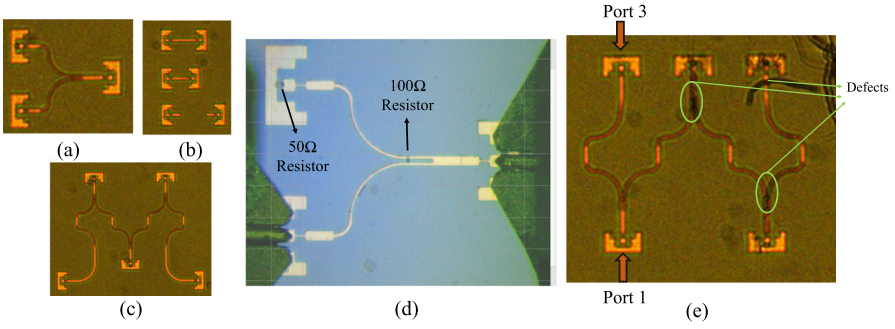

Fig. 8 Microscope screenshots of the fabricated structures. (a) WPCD, (b) TRL kit, (c) CORPS-BFN, (d) High-res picture of WPCD highlighting the position of the resistors and the placement of the probes. Microscope view of defective structures for S31 measurement

3.6 Characterization of Thin Film Resistors

The resistors included in between the outputs of the WPCD, as well as the ones acting as matched loads were implemented as monolithically integrated thin films of oxidized titanium (Ti + TiO_2) to develop integrated resistors with approximated resistance values of 100 Ω and 50 Ω. The main advantage for us in choosing Titanium was that only a single material was required to implement the resistors, in contrast to other alloys such as nichrome [52]. In addition, Ti undergoes a natural oxidation process at ambient conditions due to contact with the atmosphere with typical layer thicknesses between 3 and 7 nm [53]. Consequently, a thin layer of Titanium Oxide (mainly TiO_2) was expected to be in our samples (and in the final prototype), and therefore it would take part in the overall sheet resistance (R_s). The presence of this oxide was harnessed, since the outer oxide layer prevents further oxidation of the core material and increases the overall resistance enabling a more compact solution that fits between the output arms of the WPCD (15 µm). Several samples of Ti with different thicknesses were deposited by means of electron beam evaporation on an intrinsic, high-resistivity silicon wafer. The wafer's high resistivity is crucial to neglect its contribution to the measured sheet resistance. Otherwise, the problem must be treated as a multi-layer structure where each layer, composed of a single material, contributes with a resistance, and the measured resistance results from a parallel sum of each layer's resistances. In fact, the measured sheet resistances presented here do not correspond to Ti thin films alone. Instead, they result from a parallel sum of the resistance of a layer composed of an unknown thickness of TiO_2 and a layer of Ti with known thickness. This idea is depicted in Fig. 9. Standard photolithography was employed to create 1-cm-wide square patterns to be measured. Then, the DC R_s was measured with Ossila's Four Probe system [54]. More information regarding this method is available in [55].

The samples were measured on the same day of deposition and after a week to check if the oxidation continued. Table 3 includes the most relevant information regarding the different samples fabricated. The data shows that no significant oxidation occurred within a week after fabrication. The variations observed fall under the uncertainty of

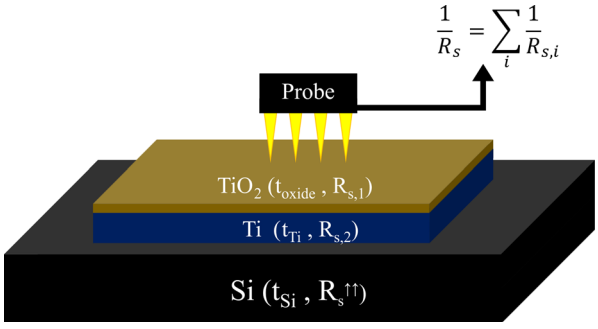

Fig. 9 Sketch of the four-point probe method for oxidized Ti thin-film sheet resistance measurements

Table 3 DC Sheet resistance of oxidized Titanium thin films

Targeted Thickness [nm]	50	100	150	200
Measured Thickness [nm]	47	93	140	187
Total samples	6	4	6	4
Max. current [mA]	20	50	100	100
Mean R_s - Day 0 [Ω/sq]	124.2	82.1	29.8	17.9
Mean R_s - Day 7 [Ω/sq]	123.2	82.5	29.5	18.1
Mean σ - Day 7 [kS/m]	174.1	129.9	243.7	297.2
Tolerance [Ω/sq]	±5	±1.5	±3	±1.5
Tolerance [kS/m]	±6.6	±2.2	±23.6	±23.4

the measurements, including an uncontrolled ambient temperature on the days the measurements were made. Each sample was measured 100 times for different maximum supported current intensities. The software provides an average value for each sample's sheet resistance (R_s), together with a tolerance. The mean values displayed here account for the average between every sample with the same thickness, whereas the tolerance value stands for the maximum difference between the measured samples and the average values. Samples with targeted thicknesses of 50, 100, 150 and 200 nm (values provided by the sensor in the e-beam evaporator) were prepared. However, SEM imaging determined that the actual thickness was slightly smaller. The conductivity values presented in the table are calculated by applying Eq. 3, where 't' is the thickness of the thin film.

$$\sigma = \frac{1}{\rho} \ [\mathrm{S/m}] \quad ; \quad \rho = R_s \cdot t \ [\Omega \cdot \mathrm{m}] \tag{3}$$

The trust in the displayed values of the 100-nm-thick samples is arguable since the conductivity obtained is lower than the one for 50 nm. In addition to the uncertainty observed in the measurements, it was assumed that such DC resistance values would be higher for a working frequency of 300 GHz, since the permittivity of conductor materials decreases with increasing frequencies, as explained by Drude's model [56]. For instance, the conductivity of copper was measured in [57], presenting half of the DC conductivity at 300 GHz. Furthermore, the roughness of the thin film would also increase the overall effective resistivity [58]. Considering this evidence and the dimensions of the WPCD, it was determined that a thickness of 200 nm would be a convenient choice, providing a DC sheet resistance of about 18.1±1.5 Ω/sq (presumably, 36 Ω/sq at 300 GHz). Given that the samples were characterized with a tolerance of more than ±20kS, a remarkable uncertainty in the value of the resistors was assumed. After assessing with EM simulations its limited influence on the performance of the WPCD, it was decided that our approach would be accurate enough for first prototype implementation, and a sheet resistance of 30± 3 Ω/sq was estimated. The actual resistance (R) of a thin-film resistor based on its length (L), width (w), and

sheet resistance of the material was calculated following Eq. 4. Hence a relatively low aspect ratio (between 4:1 and 3:1) would be required to implement a 100 Ω resistor (half the aspect ratio when addressing the 50 Ω loads)

$$R = \frac{\rho \cdot L}{w \cdot t} = R_s \cdot \frac{L}{w} \quad [\Omega] \tag{4}$$

4 Full-port Characterization of the CORPS-BFN and WPCDs

The measurements were performed with a ZVA40 Vector Network Analyzer and a pair of waveguide extenders, namely a transceiver ZC330 (Tx/Rx) and a receiver (Rx) module ZRX330, all from Rohde & Schwarz. Consequently, only S_{11} and S_{21} were available at the Devices Under Test (DUTs) in a single measurement. Since the DUTs are asymmetrical, the set-up was flipped in order to obtain the corresponding S_{22} and S_{12} parameters. Although this practice may incur an additional phase uncertainty due to different positioning of the probes within each measurement, the extraction of the whole parameter set was crucial to characterize the DUTs. A commercial waveguide TRL calibration kit was used first, to shift the measurement reference plane to the rectangular waveguide outputs and eliminate the effect of the measurement set-up and waveguide extenders. Then, the fabricated TRL calibration kit on InP was used to de-embed the probes and CPW transition effects from the measured data. As already discussed, the lumped resistors placed in the unconnected ports were not expected to work as accurate 50 Ω loads, having some deviation from the desired impedance and affecting the scattering parameters of the components. For this reason, each structure was simulated in HFSS, including lumped ports (with a PEC bridge as the one shown in Fig. 7(a)) as well as the lumped loads (Ti+TiO_2 thin films with a custom conductivity) in order to have a more realistic benchmark, to which we could compare the measured results. In these simulations, it was observed that the coplanar GND pad was introducing a frequency-dependent reactance that deviated the load impedance from the targeted 50 Ω, but overall the reflection coefficient observed at these loads was kept below -15 dB.

Figure 10 (a) to (g) present these comparisons with a sketch of the corresponding structure measured in each case. Each figure compares every measurement (two ports contacted by the probes with the rest being loaded with resistors) with its corresponding simulation after TRL de-embedding.The figures show a general agreement between measurements and simulations, where the port matching and isolation between ports remain respectively below the -10dB and -15dB benchmarks. Overall, most of the differences between measurement and simulation are due to the impossibility of emulating the GSG probe in the simulated environment. Therefore, some of these figures deserve an individual analysis.

1. It is observed that the wave port simulations (Figs. 4 and 5) and the de-embedded lumped port simulations (dotted lines in Fig. 10) show appreciable differences. This supports the idea that the load resistors are not acting as purely 50 Ω resistive loads. In addition, wave port simulations do not excite any surface mode propagating within the structure (namely TM_0, although it might be excited at dis-

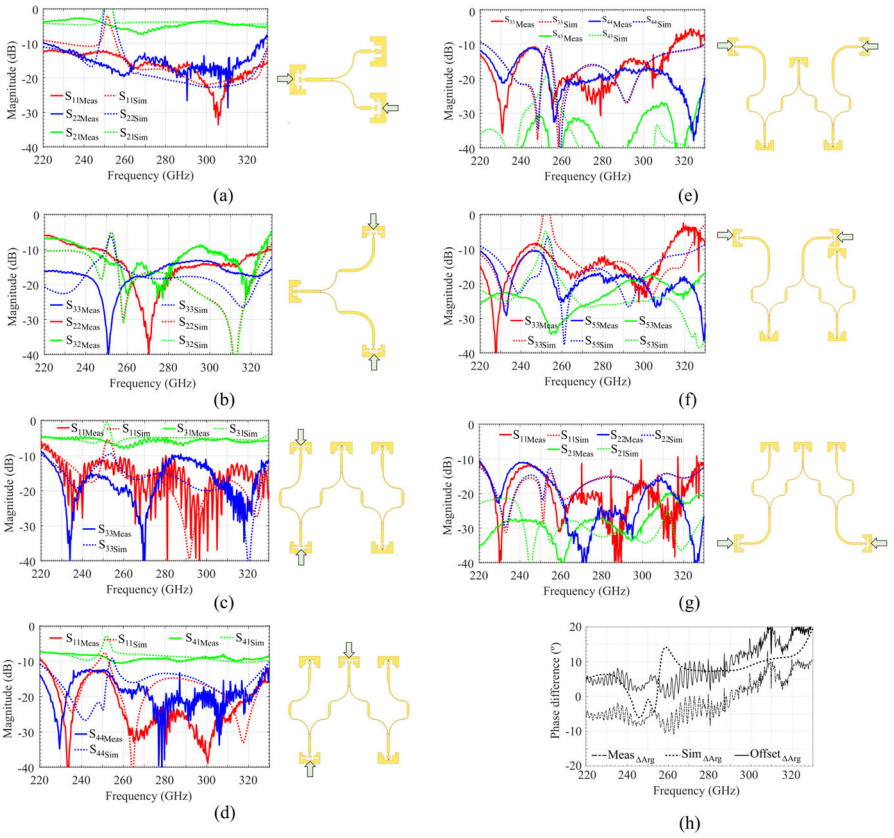

Fig. 10 Comparison between measured and simulated structures after TRL de-embedding. (a): Transmission in WPCD (P1 and 2). (b): Isolation in WPCD (P2 and 3). (c): Transmission to lateral output in CORPS-BFN (P1 and 3). (d): Transmission to central output in CORPS-BFN (P1 and 4). (e): Isolation between opposite outputs in CORPS-BFN (P3 and 5). (f): Isolation between contiguous outputs in CORPS-BFN (P3 and 4). (g): Isolation between input ports in CORPS-BFN (P1 and 2). (h): Phase difference for equivalent electrical paths (From Port 1 to Ports 3 and 4). Dotted line: simulation. Dashed line: de-embedded measurement. Solid line: Measurement after applying a positioning offset

continuities), whereas, on the contrary, this mode is generated in both lumped-port simulation and the actual measurement scenarios, mainly due to the GCPW transition. Furthermore, the coplanar transition included in the lumped port simulations alters the response.

2. It can be seen that the transmission curves (green) in sub-figures (a), (c) and (d) are affected by a slight undulation, evidencing the presence of standing waves. These standing waves were captured in the Thru standard of the TRL custom kit, and are therefore translated to the de-embedded parameters after performing the TRL de-embedding process.
3. Fig. 10 (b) denotes a notable disagreement in the isolation (green figure). This is attributed to the influence of the TM_0 mode, which couples the power between the ports due to the propagation across the substrate. Since the GSG probes could not

be modelled accurately, the power transfer to this mode due to the transition cannot be estimated in simulation. Similar conclusions can be extracted from figures (e), (f) and (g).

4. Fig. 10 (c) shows a substantial disagreement between the simulated and measured S_{33}. In this case, it was found that the structure was damaged at its opposite edge (as shown in Fig. 8 (e)), resulting in the deterioration of the reflection coefficients. The S_{11} in this case follows the trend of the simulated trace, but is severely affected by noise. This is caused by the reflections taking place at the defective part of the structure, which travel back to Port 1. On the other hand, the reflection coefficient at Port 3 is not as much affected by noise as Port 1, because it is isolated from the rest of the network thanks to the resistor in the WPCD. In this case, the curve deviates from the simulated results specially at around 290 GHz, but overall it remains below the -10 dB level. It is therefore especially worth noting the robustness of the design, with a good agreement in terms of S_{31} and both reflection coefficients remain low, thank to the intrinsic isolation of CORPS-BFN: even though one of the S-nodes on the opposite edge is defective, the rest of the network works almost unaffectedly.
5. Overall, some responses seem to be shifted towards lower frequencies, denoting that the integrated resistors have higher resistances than the designed ones. The simulations in Figs. 4 and 5 support this reasoning. In order to discard other hypotheses, the propagation constant, and the effective permittivity of the microstrip lines, were extracted from the de-embedded S_{21} measurements of some dummy lines fabricated on the wafer. These lines are shown in Fig. 11, together with the computed real (attenuation) and imaginary (phase) parts of the propagation constant, as well as the effective permittivity computed from the phase constant. The lengths highlighted in the figure are relative to the 'Thru' standard (200 µm). These magnitudes are compared with results obtained in Eigenmode simulation (see Fig. 3) for a 30-µm-wide microstrip line. A good agreement is obtained in terms of the phase constant and the effective permittivity of the lines, denoting that the InP electrical properties were simulated accurately. The attenuation constant shows relatively worse agreement, especially in the straight line, presumably due to the standing waves being formed in the Thru standard, as well as in the Straight line. The small disagreement observed in Fig. 11 (b) and (c) is mainly attributed to the influence of the TM_0 substrate mode - which is unavoidably present in the measurement, whereas the simulation reference was computed for a monomode line. Nevertheless, it can be concluded that the influence of such surface mode in this case is moderate and a good agreement with the expected propagation characteristic of the microstrip mode is achieved.
6. Most of the simulated responses show a singularity between 250–260 GHz, with the S_{21} being higher than 0 dB, which is clearly not consistent with a passive device. This is attributed to the influence of the transition, which presented a resonance around this band. This resonance becomes specially notable in the simulated parameters, where the TRL algorithm normalizes the transmission coefficient taking the Thru as a reference. In our case, the simulated Thru presented a deep resonance at this frequency, with an S_{21} of about -10 dB. However, the simulations of larger structures did not present such a deep resonance and, as a result,

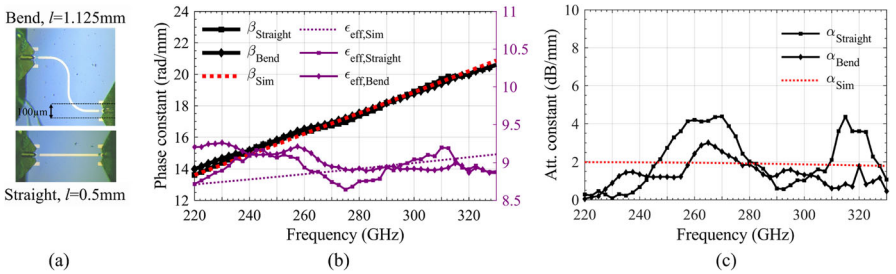

Fig. 11 (a) Dummy lines for extracting the propagation constant. (b) Phase constant (left axis) in rad/mm and effective permittivity (right). (c) Attenuation constant (dB/mm). Red lines were obtained by Eigenmode simulation

the normalization with the Thru reference creates the singularity. As such, the simulated curves in Fig. 10 shall not be considered valid between 250 and 260 GHz.

Whereas the magnitude of the S-Parameters agrees reasonably well, it was discussed earlier that the phase response of the CORPS-BFN is crucial, and that the delay suffered by the signals travelling from Port 1 to Ports 3 and 4 must be the same for optimum performance. Figure 10 (h) shows the difference in phase measured for S_{31} and S_{41} parameters. The dotted line represents the simulated phase difference for ideal resistance values and lumped-port simulations. Whereas the measured curve (dashed) seems to follow the simulated curve, with an increase with frequency, an offset of about 10° is observed. Such an offset could be due to the different positioning of the GSG probes at each measurement. As a quick calculation, this phase difference at 300 GHz for an InP-microstrip line would imply a physical length lower than 10 μm (one half per probe), which lays reasonably within the positioning accuracy of the measurement set-up. Overall, the offset curve (solid) agrees reasonably well with the simulated one (except for the region around 250–260 GHz due to the TRL algorithm).

Overall, the on-wafer characterization was affected by several factors, such as the need for a transition between different planar technologies, the need to measure 3-port and 5-port devices and the uncertainty in the thin films' sheet resistance. Nevertheless, it is concluded that despite such drawbacks, the measurements show a remarkable level of agreement with the de-embedded lumped port simulations, which aimed to reproduce the measurement scenario as accurately as possible. The challenges encountered in the measurement campaign have been identified for future studies. Overall, the insertion loss of the network ranges from 1.6 to 3.2 dB within the targeted band. In addition, it can be checked that the Wilkinson power divider fabricated here lays within the state of the art of power splitters in the sub-THz band (see Table 4), with an average insertion loss of 1 dB, which could be even lower if the distance between its output arms had not been fixed to 480 μm. This table shows that not many implementations of WPCD have been presented at these frequency ranges, and that, overall, the loss introduced by planar technologies is relatively high.

Table 4 State of the art of planar power combiners above 200 GHz

Ref	Freq(GHz)	BW (%)	IL (dB)	Isol. (dB)	RL (dB)	Type	Subs	Tech
[23]	450–600	28.6	<1	>20	>10	WPCD	Si	Stripline
[43]	310–330	6.25	≈ 1.7	N/A	N/A	WPCD	Si	CPW*
[59]	220–320	37	≈ 0.7	N/A	>13	Y Junc	InP	μstrip
[60]	600–700	15.4	≈ 0.3	N/A	N/A	Y Junc	Air	Hollow WG
[61]	220–330	40	1–3	N/A	<10	Y Junc	Air	Par. Plate
[62]	210–230	9.1	≈ 0.8	N/A	N/A	Y Junc	InP	μstrip*
[63]	220–320	37	≈ 1.2	N/A	>15	Y Junc	InP	Coup. CPW
[64]	220–320	37	≈ 1	N/A	N/A	Y Junc	InP	μstrip/slot
[65]	630–750	17.4	1–2	>20	>20	Hyb. 90°	SOI	μstrip*
[66]	200–400	66.7	<1	>13	>15	WPCD	GaAs	El. CPW*
[66]	200–400	66.7	<1	>12	>14	WPCD	BCB	μstrip*
[67]	630–670	6.15	<0.5	N/A	N/A	Y Junc	Si_3N_4	CPS*
This Work	220–330	40	<1	>13	>13	WPCD	InP	μstrip
This Work	270–320	16.9	<1	>17	>17	WPCD	InP	μstrip

*Simulation

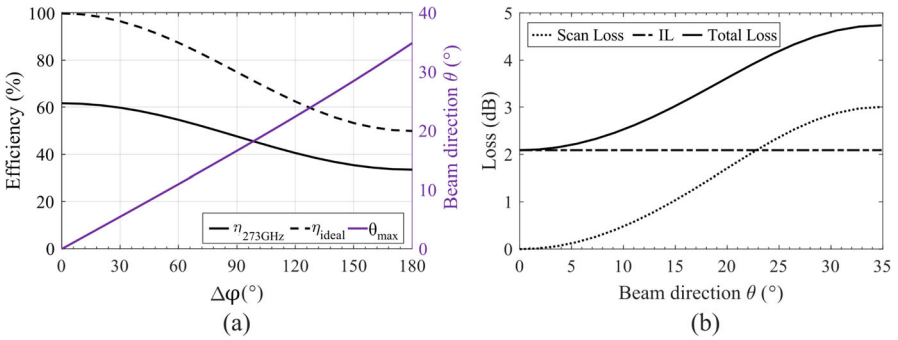

Fig. 12 Efficiency and scanning capabilities. (a) Efficiency is the fabricated (solid) and ideal (dashed) CORPS-BFN vs achievable beam deflection. (b) Overall loss of the presented THz CORPS-BFN @273 GHz for different beam directions

5 Applications and Scalability

In our recent work [33] we demonstrated a 2D beam steering approach in the WR3.4 band enabled by the joint operation of a 3-element leaky wave antenna (LWA) array and a 2×3 CORPS-BFN. The BFN in [33] presented a modified output impedance to match the input impedance of the antennas used ($\sim$40 Ω), and therefore the microstrip delay lines and the WPCD implementing the R-node were slightly different. The simulated performance of the network in [33] considering the IL, the isolation between input ports and the port matching was similar to the one characterized here. The proposed solution allowed controlling the beam orientation was controlled by only two parameters: the frequency of operation and a time delay implemented by an optical delay line. The frequency defined mainly the beam direction in elevation (θ) for the LWAs within the H-plane, whereas the azimuth (ϕ) angle within the E-plane was determined by the time delay (phase shift) between the input ports, which together with the CORPS-BFN delivered a linearly progressive phase distribution to the antennas. Overall, the number of phase shifters (PS) required to perform the beam steering with three antennas was reduced thanks to the CORPS-BFN. However, no actual characterization of the BFN was provided in the previous study, and this information is essential to perform an objective analysis on the performance of the network and its potential applications. Concerning the measured S-parameters of the network, its measured insertion loss ranges from 1.6 dB to 3.2 dB across the WR3.4 band. The 2×3 CORPS-BFN operates both ports together at the same time in beam-steering application. As such, if an efficiency was defined as the ratio of power delivered to the antenna ports, considering a normalized power of 1 W on each input port, we would obtain a maximum and minimum efficiency of about 70% at 233 GHz and 48% at 330 GHz, respectively, for a boresight radiation (no phase difference between the inputs). At 275 GHz, the centre of the band, the efficiency is about 61.8% (2.1dB IL). However, this efficiency experiences a penalty when steering the beam (scan loss) due to the phase difference between the input signals. This is depicted in Fig. 12, where the efficiency and the scanning range of the proposed network are interrelated.

In conclusion, this beam steering solution trades-off system complexity (reduced number of PS) and efficiency. On the one hand, it allows feeding up to 3 antennas with just two PS (actually, only one PS could be enough if the phase is calibrated beforehand). On the other hand, the the scan loss can limit the steering range of the system. In addition, as explained in Sect. 2, the use of a higher number of layers does not seem convenient, as the network would introduce additional loss and halve its scanning range. Conversely, the most convenient approach is to operate several 2×3 CORPS-BFN blocks in parallel, as shown in Fig. 13, where the array factor of 3 blocks operating together is also provided to illustrate the benefits of this approach. Adding blocks in parallel does not decrease the efficiency of the network, but allows feeding a higher number of antennas at the same time the required number of PS is reduced up to a 33% in comparison to an individual PS/antenna approach. In addition, the use of several blocks improves the radiation characteristics when higher phase shifts are applied (the side lobe level is reduced with an increasing number of blocks).

As for a multi-beam application of the CORPS-BFN, sketched in Fig. 2 (a), one practical sample scenario at THz frequencies would be in a THz imaging system. It is widely known that operating at higher frequencies provides a finer resolution due to the lower wavelength employed. However, once the wavelength is fixed (for instance, 1 mm at 300 GHz), increasing the resolution of the system is challenging. Each pixel will be resolved if enough power is received by the detector and if the Signal-to-Noise Ratio (SNR) is sufficiently high. If each pixel is resolved by a single detector and a single antenna, the distance between the pixels that can be detected will be the distance between the antennas. However, small antennas close to each other do not offer higher gains, thus, they might not collect enough power to resolve the pixel successfully. In order to achieve a higher SNR, an antenna with a higher gain can be employed. However, this implies an electrically larger antenna, hence increasing the distance between the pixels. In this context, the CORPS-BFN would allow sharing multiple antenna elements between neighbouring pixels. Each pixel uses L+1 antennas in this case, where L is the number of layers in the CORPS. Thus, each pixel uses an antenna array, instead of a single antenna, to capture the power. The neighbouring pixel uses L+1 antennas as well, most of which (L) are shared with the contiguous pixels. As a result, the effective distance between the pixels remains as low as the distance between the antennas, at the same time the SNR is increased [68]. In addition, since the antenna

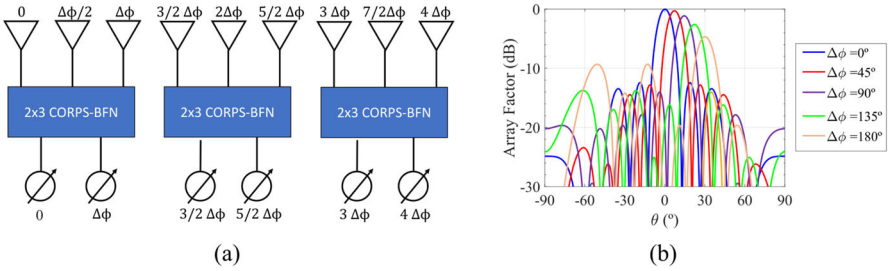

Fig. 13 Parallel operation of 2×3 CORPS-BFN blocks (a) Sketch. (b) Normalized array factor for beam steering application

array provides a narrower beam, the angular resolution of the system can be enhanced. Additionally, CORPS-BFN could be used in a quasi-optical system to feed a reflector or a lens, generating beams in different directions due to the relative offset position of the antenna elements from the system's focus, such as in [21].

However, the main concern here would be the efficiency, as each input port operates individually. Thus, the efficiency reported in Fig. 12 (for the boresight direction) would be halved, since there is no power combination in the R-nodes of the first layer. In order to overcome this limitation, more efficient topologies were proposed in [39], where the authors conceived newer configurations with significantly higher efficiencies by removing some of the S-/R-nodes. These configurations, which exchange a higher efficiency with a reduced overlapping ratio between the generated beams, may be an interesting choice for future implementations due to the limited power available at THz systems nowadays.

6 Conclusion and Outlook

In this work, a detailed description of the design, fabrication and characterization of CORPS-BFN for operation at the WR3.4 THz band has been provided, including the implementation of monolithically integrated thin film resistors based on Titanium thin films, which constitute a convenient solution due to their simple manufacturing process. For their implementation, their natural oxidation at ambient conditions has been harnessed. Overall, a remarkable agreement between simulations and measurements has been achieved, with an isolation between input ports better than 20 dB and a reflection coefficient better than -15dB in most part of the band, taking into account that modelling the GSG probes in simulation was a challenging task. A procedure to characterize multi-port networks by introducing monolithically integrated lumped loads has been proposed. In addition, the functionalities of this type of beam forming network have been discussed and its scalability and potential applications at this frequency regime has been assessed.

Concerning future research, whereas this prototype serves as proof of concept for Terahertz frequencies, further efforts should address ways to reduce the insertion loss of the network (between 1.6 and 3.2 dB), which reduce its efficiency. As such, technologies other than microstrip shall be explored in the future. In addition, ways to perform a more accurate characterization of the thin-films implementing the resistors should be adopted, to further improve the network performance and the reliability of the design stage. If these matters are addressed properly, CORPS-BFN should prove themselves useful in various scenarios and applications. For instance, those requiring a beam steering capability with a limited scanning range ($\pm$20–30°), such as short-range communications, allowing a certain degree of user mobility, or chip-to-chip wireless interconnects [69]. On the other hand, the joint operation of a THz CORPS-BFN and a quasi-optical element (lens, reflector) to implement an overlapped multi-beam system, or its use in other imaging schemes is yet to be demonstrated in this frequency regime, being specially interesting to study the configurations proposed in [39] for an enhanced efficiency. Such a demonstration looks promising, as it may push the resolution of THz systems even further. Moreover, the implementation of the BFN on

an InP substrate contributes in paving the wave towards the monolithic integration of III-V THz sources with antenna arrays.

Acknowledgements C.B.Q would like to thank Dr Omar Fuentes Lorenzo and the Sensors Group at UPNA for allowing the use of the Four-Probe resistivity measuring equipment. The authors would also like to thank the reviewers for their valuable suggestions

Author Contributions C. Biurrun-Quel envisioned the design, performed the simulations, fabricated the prototype, wrote the main manuscript text and ellaborated the figures. T. Haddad assisted in the manuscript's writing, as well as during the design, simulation and experiment stages. B. Sievert and R. Kress performed the experiments, together with T. Haddad. N. Weimann, D. Erni, A. Rennings, A. Stöhr, J. Teniente, and C. del-Río provided guidance prior to, during, and after the experiment, as well as during the elaboration of the manuscript. They obtained the sources of funding as well. All authors reviewed the manuscript thoroughly in every stage

Funding This research was funded partially by the FPU Program from the Spanish Ministry of Science and Innovation, grant No. FPU18/00013, and project PID2019-109984RB-C43 (FRONT-MiliRAD); by the Deutsche Forschungs-Gemeinschaft (DFG, German Research Foundation) under Project 287022738-CRC/TRR 196 MARIE (Projects C02, C05, C06, C07 and S03); by BMBF (smartBeam, 6GEM grant No. EFRE-0400215, grant No.16KISK017 and grant No.16KISK039) and by the NRW/EFRE Terahertz-Integrationszentrum (Open6GHub and THz.NRW). Open Access funding provided by Universidad Pública de Navarra.

Data Availability Not applicable.

Declarations

Conflicts of interests The authors declare that they have no conflict of interest

Ethical Approval Not applicable

References

1. T. Nagatsuma, H. Ito, T. Ishibashi, Laser and Photonics Reviews **3**(1-2), 123 (2009). https://doi.org/10.1002/lpor.200810024
2. L. Duvillaret, F. Garet, J.L. Coutaz, IEEE Journal on Selected Topics in Quantum Electronics **2**(3), 739 (1996). https://doi.org/10.1109/2944.571775
3. K. Humphreys, J. Loughran, M. Gradziel, W. Lanigan, T. Ward, J. Murphy, C. O'Sullivan, in *The 26th Annual International Conference of the IEEE Engineering in Medicine and Biology Society*, vol. 3,(IEEE, 2004), vol. 3, pp. 1302–1305. https://doi.org/10.1109/IEMBS.2004.1403410
4. D.M. Mittleman, R.H. Jacobsen, M.C. Nuss, IEEE Journal on Selected Topics in Quantum Electronics **2**(3), 679 (1996). https://doi.org/10.1109/2944.571768

5. H.B. Liu, H. Zhong, N. Karpowicz, Y. Chen, X.C. Zhang, in *Proceedings of the IEEE*, vol. 95 (Institute of Electrical and Electronics Engineers Inc., 2007), vol. 95, pp. 1514–1527.https://doi.org/10.1109/JPROC.2007.898903
6. S. Koenig, D. Lopez-Diaz, J. Antes, F. Boes, R. Henneberger, A. Leuther, A. Tessmann, R. Schmogrow, D. Hillerkuss, R. Palmer, T. Zwick, C. Koos, W. Freude, O. Ambacher, J. Leuthold, I. Kallfass, Nature Photonics **7**(12), 977 (2013). https://doi.org/10.1038/nphoton.2013.275
7. H.J.J. Song, T. Nagatsuma, IEEE Transactions on Terahertz Science and Technology **1**(1), 256 (2011). https://doi.org/10.1109/TTHZ.2011.2159552
8. T. Kleine-Ostmann, T. Nagatsuma, Journal of Infrared, Millimeter, and Terahertz Waves **32**(2), 143 (2011). https://doi.org/10.1007/s10762-010-9758-1
9. H.J. Song, N. Lee, IEEE Transactions on Terahertz Science and Technology pp. 1–1 (2021). https://doi.org/10.1109/TTHZ.2021.3128677
10. R.A. Lewis, Journal of Physics D: Applied Physics **47**(37), 374001 (2014). https://doi.org/10.1088/0022-3727/47/37/374001
11. R.E. Miles, P. Harrison, D. Lippens, *Terahertz Sources and Systems* (Springer Netherlands, 2012).https://doi.org/10.1007/978-94-010-0824-2
12. D. Headland, Y. Monnai, D. Abbott, C. Fumeaux, W. Withayachumnankul. Tutorial: Terahertz beamforming, from concepts to realizations (2018). https://doi.org/10.1063/1.5011063
13. J. Blass, in *1958 IRE International Convention Record* (IEEE, New York, 2005), pp. 48–50. https://doi.org/10.1109/irecon.1960.1150892
14. J. Butler, R. Low, Electronic Design **9**, 170 (1961)
15. M. Elkhouly, Y. Mao, C. Meliani, J.C. Scheytt, F. Ellinger, IEEE Journal of Solid-State Circuits **49**(9), 1916 (2014). https://doi.org/10.1109/JSSC.2014.2317147
16. Y.J. Guo, M. Ansari, R.W. Ziolkowski, N.J. Fonseca, IEEE Open Journal of Antennas and Propagation **2**, 807 (2021). https://doi.org/10.1109/OJAP.2021.3093622
17. W. Rotman, R.F. Turner. Wide-Angle Microwave Lens for Line Source Applications (1963). https://doi.org/10.1109/TAP.1963.1138114
18. D. Headland, W. Withayachumnankul, R. Yamada, M. Fujita, T. Nagatsuma, APL Photonics **3**(12), 126105 (2018). https://doi.org/10.1063/1.5060631/1.5060631.MM.ORIGINAL.V2.MPG
19. M. Alonso-Delpino, C. Jung-Kubiak, T. Reck, N. Llombart, G. Chattopadhyay, IEEE Transactions on Terahertz Science and Technology **9**(1), 47 (2019). https://doi.org/10.1109/TTHZ.2018.2881930
20. D. Betancourt, C. Del Río, in *European Space Agency, (Special Publication) ESA SP*, vol. 626 SP (European Space Agency, 2006), vol. 626 SP. https://doi.org/10.1109/eucap.2006.4584954
21. Q. Garcia, L. Orgaz, J. Del Castillo, G. Toso, E. Imbembo, C. Biurrun-Quel, C. Del Rio, N. Memeletzoglou, IEEE Antennas and Wireless Propagation Letters **20**(11), 2110 (2021). https://doi.org/10.1109/LAWP.2021.3102868
22. X.D. Deng, Y. Li, J. Li, C. Liu, W. Wu, Y.Z. Xiong, IEEE Transactions on Terahertz Science and Technology **5**(6), 930 (2015). https://doi.org/10.1109/TTHZ.2015.2477604
23. P. Hillger, R. Jain, J. Grzyb, W. Forster, B. Heinemann, G. MacGrogan, P. Mounaix, T. Zimmer, U.R. Pfeiffer, IEEE Journal of Solid-State Circuits **53**(12), 3599 (2018). https://doi.org/10.1109/JSSC.2018.2878817
24. X. Zhang, F. Fan, C.Y. Zhang, Y.Y. Ji, X.H. Wang, S.J. Chang, Optical Materials Express **10**(2), 282 (2020). https://doi.org/10.1364/ome.383058
25. S. Li, J. Wang, H. Tian, L. Li, J. Liu, G.C. Wang, J. Gao, C. Hu, Z. Zhou, Optics Letters **45**(10), 2834 (2020). https://doi.org/10.1364/ol.393571
26. B.S. Ung, X. Liu, E.P. Parrott, A.K. Srivastava, H. Park, V.G. Chigrinov, E. Pickwell-Macpherson, IEEE Transactions on Terahertz Science and Technology **8**(2), 209 (2018). https://doi.org/10.1109/TTHZ.2018.2790708
27. H. Afzal, R. Abedi, R. Kananizadeh, P. Heydari, O. Momeni, IEEE Transactions on Microwave Theory and Techniques **69**(2), 1439 (2021). https://doi.org/10.1109/TMTT.2020.3039517
28. P. Huggard, B. Ellison, P. Shen, N. Gomes, P. Davies, W. Shillue, A. Vaccari, J. Payne, Electronics Letters **38**(7), 327 (2002). https://doi.org/10.1049/el:20020202
29. B. Vidal, T. Mengual, C. Ibáñez-López, J. Marti, IEEE Photonics Technology Letters **18**(24), 2590 (2006). https://doi.org/10.1109/LPT.2006.887347
30. Q. Cheng, S. Zheng, Q. Zhang, J. Ji, H. Yu, X. Zhang, Optics Communications **489**, 126809 (2021). https://doi.org/10.1016/j.optcom.2021.126809

31. D. Betancourt, C. del Rio Bocio, C. del Río Bocio, IEEE Transactions on Antennas and Propagation **55**(9), 2489 (2007). https://doi.org/10.1109/TAP.2007.904133
32. D. Betancourt, C. Del Río, in *29th ESA Antenna Workshop on Multiple Beams and Reconfigurable Antennas* (Noordwijk, 2007)
33. T. Haddad, C. Biurrun-Quel, P. Lu, J. Tebart, B. Sievert, S. Makhlouf, M. Grzeslo, J. Teniente, C. Del-Rio-Bocio, A. Stohr, Optics Express, Vol. 30, Issue 21, pp. 38596-38612 **30**(21), 38596 (2022). https://doi.org/10.1364/OE.468200
34. A. Ibanez, R. Garcia, D. Betancourt, C. Del-Rio, in *ANTEM 2005 - 11th International Symposium on Antenna Technology and Applied Electromagnetics, Conference Proceedings* (Institute of Electrical and Electronics Engineers Inc., 2005). https://doi.org/10.1109/ANTEM.2005.7852092
35. D. Betancourt, C. Del Río, Microwave and Optical Technology Letters **48**(8), 1599 (2006). https://doi.org/10.1002/mop.21697
36. E.J. Wilkinson, IRE Transactions on Microwave Theory and Techniques **8**(1), 116 (1960). https://doi.org/10.1109/TMTT.1960.1124668
37. U. Gysel, in *IEEE-MTT-S International Microwave Symposium* (Institute of Electrical and Electronics Engineers (IEEE), 1975), pp. 116–118. https://doi.org/10.1109/mwsym.1975.1123301
38. C. A. Balanis, *Antenna Theory: Analysis and Design* (John Wiley & Sons 2016)
39. N. Ferrando, N.J. Fonseca, IEEE Transactions on Antennas and Propagation **59**(2), 493 (2011). https://doi.org/10.1109/TAP.2010.2096392
40. J.A. Hejase, P.R. Paladhi, P.P. Chahal, IEEE Transactions on Components, Packaging and Manufacturing Technology **1**(11), 1685 (2011). https://doi.org/10.1109/TCPMT.2011.2163632
41. D.M. Pozar, IEEE Transactions on Antennas and Propagation **31**(5), 740 (1983). https://doi.org/10.1109/TAP.1983.1143124
42. H. Ito, S. Kodama, Y. Muramoto, T. Furuta, T. Nagatsuma, T. Ishibashi, IEEE Journal of Selected Topics in Quantum Electronics **10**(4), 709 (2004). https://doi.org/10.1109/JSTQE.2004.833883
43. J. Lee, M. Kim, K. Yang, IEEE Transactions on Terahertz Science and Technology **6**(2), 336 (2016). https://doi.org/10.1109/TTHZ.2015.2509358
44. M. Urteaga, Z. Griffith, M. Seo, J. Hacker, M.J. Rodwell, Proceedings of the IEEE **105**(6), 1051 (2017). https://doi.org/10.1109/JPROC.2017.2692178
45. F. Huber, IEEE Transactions on Component Parts **11**(2), 38 (1964). https://doi.org/10.1109/TCP.1964.1134997
46. D. Pozar, in *Microwave Engineering*, 4th edn. (Wiley, 2011), chap. 5
47. ANSYS HFSS software. https://www.ansys.com/products/electronics/ansys-hfss
48. PathWave Advanced Design System (ADS). https://www.keysight.com/zz/en/products/software.html
49. E. Carlsson, S. Gevorgian, IEEE Transactions on Microwave Theory and Techniques **47**(8), 1544 (1999). https://doi.org/10.1109/22.780407
50. G.F. Engen, C.A. Hoer, IEEE Transactions on Microwave Theory and Techniques **27**(12), 987 (1979). https://doi.org/10.1109/TMTT.1979.1129778
51. P. Lu, T. Haddad, B. Sievert, B. Khani, S. Makhlouf, S. Dülme, J.F. Estévez, A. Rennings, D. Erni, U. Pfeiffer, A. Stöhr, IEEE Transactions on Terahertz Science and Technology **11**(2), 218 (2021). https://doi.org/10.1109/TTHZ.2020.3039460
52. E. Bloch, D. Mistele, R. Brener, C. Cytermann, A. Gavrilov, D. Ritter, Semiconductor Science and Technology **26**(10), 105004 (2011). https://doi.org/10.1088/0268-1242/26/10/105004
53. G. Wang, J. Li, K. Lv, W. Zhang, X. Ding, G. Yang, X. Liu, X. Jiang, Scientific Reports **6**(1), 1 (2016). https://doi.org/10.1038/srep31769
54. Four-Point Probe | Resistivity & Conductivity Measurement | Ossila. https://www.ossila.com/products/four-point-probe-system
55. F.M. Smits, Bell System Technical Journal **37**(3), 711 (1958). https://doi.org/10.1002/j.1538-7305.1958.tb03883.x
56. N.W.A. Mermin, N. D., *Solid State Physics* (Holt-Saunders, 1976)
57. M.P. Kirley, J.H. Booske, IEEE Transactions on Terahertz Science and Technology **5**(6), 1012 (2015). https://doi.org/10.1109/TTHZ.2015.2468074
58. M.P. Kirley, N. Carlsson, B.B. Yang, J.H. Booske, in *2012 IEEE 13th International Vacuum Electronics Conference, IVEC 2012* (2012), pp. 239–240. https://doi.org/10.1109/IVEC.2012.6262147
59. J. Kim, S. Jeon, M. Kim, M. Urteaga, J. Jeong, IEEE Transactions on Terahertz Science and Technology **5**(2), 215 (2015). https://doi.org/10.1109/TTHZ.2014.2387259

60. V. Radisic, K.M. Leong, X. Mei, S. Sarkozy, W. Yoshida, W.R. Deal, IEEE Transactions on Microwave Theory and Techniques **60**(3), 724 (2012). https://doi.org/10.1109/TMTT.2011.2176503
61. K.S. Reichel, R. Mendis, D.M. Mittleman, International Conference on Infrared, Millimeter, and Terahertz Waves, IRMMW-THz **11** (2016). https://doi.org/10.1109/IRMMW-THZ.2016.7758604
62. T.B. Reed, Z. Griffith, P. Rowell, M. Field, M. Rodwell, Technical Digest - IEEE Compound Semiconductor Integrated Circuit Symposium, CSIC (2013). https://doi.org/10.1109/CSICS.2013.6659187
63. V. Radisic, W.R. Deal, K.M. Leong, X.B. Mei, W. Yoshida, P.H. Liu, J. Uyeda, A. Fung, L. Samoska, T. Gaier, R. Lai, IEEE Transactions on Microwave Theory and Techniques **58**(7 PART 2), 1903 (2010). https://doi.org/10.1109/TMTT.2010.2050105
64. H. Yu, S. Jeon, S. Choi, M. Kim, Electronics Letters **50**(5), 377 (2014). https://doi.org/10.1049/el.2013.3288
65. B.K. Tan, G. Yassin, P. Grimes, K. Jacobs, S. Withington, IEEE Transactions on Terahertz Science and Technology **3**(1), 32 (2013). https://doi.org/10.1109/TTHZ.2012.2235527
66. L. John, A. Tessmann, A. Leuther, P. Neininger, T. Merkle, T. Zwick, IEEE Transactions on Terahertz Science and Technology **10**(3), 309 (2020). https://doi.org/10.1109/TTHZ.2020.2965808
67. W. Gomaa, R.L. Smith, H. Esmaeilsabzali, T.E. Darcie, IEEE Access **8**, 214425 (2020). https://doi.org/10.1109/ACCESS.2020.3040986
68. C. Biurrun-Quel, C. Del-Rio, 2022 52nd European Microwave Conference (EuMC) pp. 365–368 (2022). https://doi.org/10.23919/EUMC54642.2022.9924410. https://ieeexplore.ieee.org/document/9924410/
69. R.S. Narde, N. Mansoor, A. Ganguly, J. Venkataraman, in *12th European Conference on Antennas and Propagation (EuCAP 2018)* (2018), pp. 1–5. https://doi.org/10.1049/cp.2018.0959